

Effects of hygrothermal aging on anisotropic conductive adhesive joints: experiments and theoretical analysis

Y. C. LIN^{1,2}, X. CHEN^{1,*} and Z. P. WANG³

¹ *School of Chemical Engineering & Technology, Tianjin University, Tianjin 300072, P.R. China*

² *School of Mechanical and Electrical Engineering, Central South University, Changsha 410083, P.R. China*

³ *China Technology Center, Philips Mobile Display Systems, Shanghai 200131, P.R. China*

Received in final form 5 July 2006

Abstract—Epoxy-based anisotropic conductive adhesive film (ACF) joints have been used in a number of interconnect applications, including direct chip attachment, i.e., chip on glass, chip on ceramics, etc. The ACF joints can be subjected to high relative humidity environment and are susceptible to moisture sorption, especially at elevated temperatures. The long-term hygrothermal aging will induce irreversible changes to epoxy resin systems due to susceptibility of the polymer resin to hydrolysis, oxidation, etc. In this study, the hygrothermal environment was used as an accelerator for the degradation of ACF joints in chip-on-glass (COG) assemblies, which were fabricated in the form of single-lap joints. The effects of aging on the epoxy-based ACF joints were characterized by shear tests and scanning electron microscopy (SEM) at accelerated aging times of 125, 250, 375 and 550 h. The results show that the strength of ACF joints decreases and the fracture mechanism gradually changes with hygrothermal aging. In order to further interpret the hygrothermally-induced degradation to the ACF joints, an ACF joint aging model with hygrothermal environment has been developed, introducing a dimensionless parameter A , which was obtained from the interfacial fracture energy.

Keywords: Anisotropic conductive film; hygrothermal aging; chip-on-glass (COG); interfacial fracture energy.

1. INTRODUCTION

The increasing demand for higher display information density, higher resolution and maximum viewing ratio *versus* outside dimensions for mobile devices is driving

*To whom correspondence should be addressed. Tel.: (86-22) 8789-3037/2740-8399. Fax: (86-22) 8789-3037. E-mail: xchen@tju.edu.cn

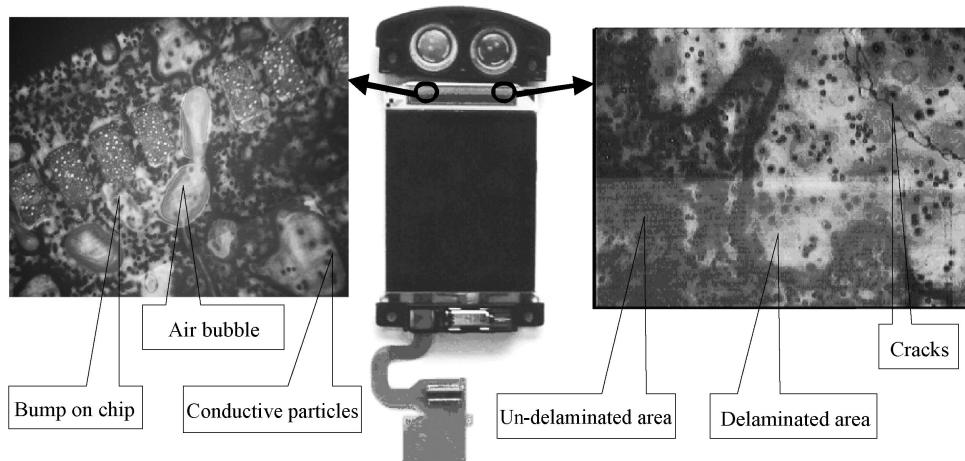


Figure 1. Various failure possibilities for a COG assembly in a mobile telephone under hygrothermal conditions.

chip-on-glass (COG) interconnections towards finer pitch, smaller contact area and higher pin counts. The most common COG technology currently used in display applications is based on anisotropic conductive adhesive films (ACFs). An ACF is a composite composed of fine conductive particles that are uniformly dispersed in the thermosetting epoxy matrix, and it has been widely used for interconnecting microelectronic elements [1–4]. The principle of COG bonding using an ACF is that the electrical connections are established through conductive particles and the mechanical interconnections are maintained by the cured adhesive. However, the epoxy-based ACF joints are often subjected to hygrothermal environments and are susceptible to moisture sorption, which is one of the major reliability concerns for the COG assembly. Prolonged hygrothermal aging may lead to irreversible degradation to the epoxy resin system due to susceptibility of the resin polymer to hydrolysis and oxidation, as well as due to the change in the effective average cross-link molecular weight. The absorbed moisture has deleterious effects on the physical properties of epoxies and can, therefore, greatly compromise the performance of an epoxy-based component. Figure 1 shows possible failures of a COG assembly in a mobile telephone under hygrothermal conditions. Obviously, the cracks and delaminations, along with some air bubbles, can be easily found at the interface between the chip and glass substrate. Some researchers have studied the effect of moisture on the epoxy resin properties, including tensile strength, elastic modulus, etc. [5–9]. For example, the influence of aging in a high temperature and high humidity environment on the adhesion performance of an underfill material (epoxy cured with acid anhydride) to the passivation layer in flip-chip packaging has been discussed [10, 11]. Meanwhile, finite element stress analysis and strength evaluation of adhesive joints of dissimilar adherends subjected to various loadings, such as tensile loads, impact bending moments, impact loads and impact tensile loads, have been carried out [12–15]. However, further investigations of ACF joints

used in COG assemblies under a humid environment with elevated temperature are greatly needed.

In this work, a hygrothermal environment (85°C/85% RH) was used as an accelerator for the degradation of ACF joints in the COG assemblies, which were fabricated in the form of single-lap joints. The effects of aging on the epoxy-based ACF joints were characterized by shear tests and scanning electron microscopy (SEM) at accelerated aging times of 125, 250, 375 and 550 h. In order to interpret the hygrothermally-induced degradation, a mechanics model is established through introducing a dimensionless parameter A , which was obtained from the interfacial fracture energy.

2. EXPERIMENTAL

2.1. Interconnection principle of ACF joints and preparation of samples

Figure 2 shows a typical COG process based on ACF interconnection techniques. First, an ACF is laminated to a glass substrate with ITO (indium tin oxide) tracks. Pressure and temperature are applied during the lamination process to ensure positioning accuracy, uniformity, etc. Then, the bumps on integrated circuits (ICs) are aligned with the tracks on the glass. Finally, the IC chip is pressed onto the glass at a specified high temperature and pressure. The conductive particles are trapped between the bumps and tracks, while the adhesive resin is squeezed out. The

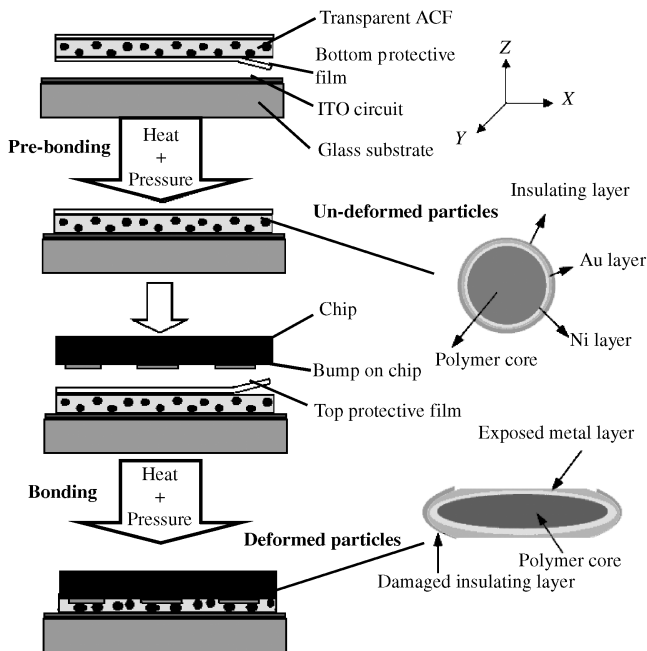


Figure 2. Interconnection process for a COG assembly.

Table 1.
Bonding process parameters

Process parameter	Preliminary bonding	Final bonding
Bonding temperature (°C)	70–80	220
Bonding pressure (MPa), per unit area of bump	5	100
Bonding time (s)	1–2	6

interconnections are established by the compressive force between the electrodes due to the shrinkage of the adhesive after curing. Consequently, the electrical conduction is restricted to the z -direction and the electrical isolation is maintained in the x - y plane.

Additionally, it is necessary to know the deformation of conductive particles during die mounting process. Generally, the conductive particles consist of a polymer core material coated with a thin metal layer (nickel or/and gold), and then insulated again with a polymer material on its exterior surface. The conductive particles in an ACF are of ball shape before die bonding. When the IC chip is pressed onto the glass at a high temperature and pressure, the particles are entrapped and deformed between the bumps of the chip and the glass substrate, and then the external insulation layer of the particle is damaged and the interior metal layer is exposed. Thus, the electrical connections are established through conductive particles.

In order to remove any contaminants, all ITO glass substrates were carefully cleaned using acetone prior to bonding. The bonding process of a COG assembly includes two main steps. The first step is the preliminary bonding, which consists of cutting the ACF into correct size to cover the bonding area and bonding the ACF onto the glass substrate. The second step is the final bonding, which bonds the chip onto the ACF-laminated glass substrate by applying heat and pressure simultaneously for a specific duration after the substrate pattern and the position of the chip bumps have been aligned. The bonding processes were completed by a special flip chip bonder, and the specific bonding process parameters used in this study are shown in Table 1.

2.2. Hygrothermal conditions and shear test

An elevated temperature and relative humidity (RH) environment can accelerate many failure mechanisms of ACF joints. In this study, a typical hygrothermal environment, 85°C/85% RH, was used as an accelerator for the degradation of ACF joints in the COG assemblies. Generally, hygrothermal aging refers to the process in which the deterioration of the mechanical performance and integrity of composite materials results from the combined action of moisture and temperature. In order to investigate the effects of hygrothermal aging on the adhesion strength, shear tests were carried out on the COG specimens, at aging times of 0, 125, 250, 375 and 550 h. These tests were performed at room temperature by a mechanically

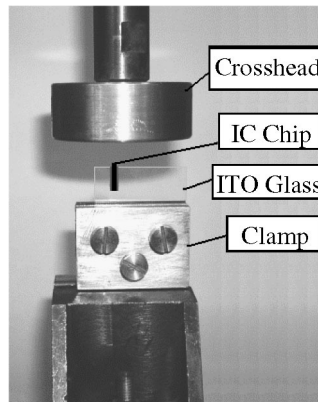


Figure 3. COG specimen loaded in a shear-test machine.

driven test machine and a cross-head speed of 1 mm/min. The experimental setup is shown in Fig. 3. Additionally, the fracture surfaces were observed by scanning electron microscopy (SEM) to further investigate the effects of hygrothermal aging on the fracture mechanisms.

3. RESULTS AND DISCUSSION

3.1. Shear test results

Figure 4 shows the relation between shear force and crosshead displacement with aging time. From the experimental results, it can be easily seen that the force increased linearly with displacement for almost all the COG specimens, and the viscoelastic deformations were insignificant. The maximum shear force prior to fracture is about 448 N at a displacement of 0.192 mm for the unaged samples. Due to the effect of elevated temperature and relative humidity (RH), the adhesion strength and displacement of COG assembly decreased with the increase of hygrothermal aging time. Moreover, the adhesion strengths of the aged COG specimens, relative to the unaged ones, are reduced by 6.5, 18.5, 23.6 and 35.0%, corresponding to hygrothermal aging times of 125, 250, 375 and 550 h, respectively.

In previous investigations [6–8], the effects of the hygrothermal aging on epoxy systems were investigated by the uniaxial tensile test, scanning electron microscopy (SEM) analysis, computer simulation and molecular dynamics method. The results showed that, due to the plasticization effect of absorbed moisture, both the tensile elastic modulus and tensile strength of the epoxy system studied were reduced, i.e., the absorbed moisture had deleterious effects on the physical properties of epoxies and can, therefore, greatly compromise the performance of an epoxy-based component. Additionally, the fracture mechanism of epoxy system was altered. It is well known that the solubility-diffusivity behavior of small molecules (e.g., water) in the polymer matrix generally has a strong relation with the glass-transition

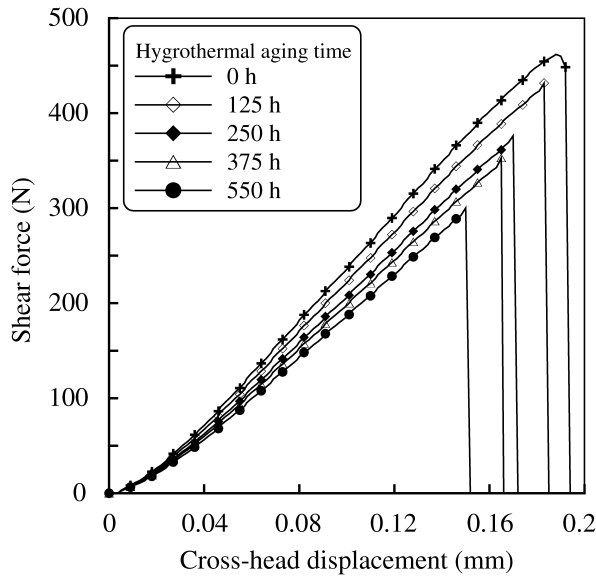


Figure 4. Shear force–cross-head displacement curves for various hydrothermal aging times (bond length, $L = 6.5$ mm).

temperature (T_g) of the polymer, and the effects of hydrothermal aging on the T_g were investigated by some researchers [16, 17]. The T_g of the epoxy resin will decrease under a humid environment along with high temperature. Absorbed moisture can attack the cross-link chains in an epoxy resin, causing chain scission and leaching of segments. Generally, the T_g can be related to the cross-link density. With a decrease of cross-link density, the T_g decreases as well. In other words, the hydrothermal aging induces irreversible damage to the epoxy system, physically (plasticization, as well as the formation of cracks and crazes) and/or chemically (hydrolysis). Furthermore, the absorbed moisture can attack the adhesive/inorganic substrate interfaces and the hydrolysis will occur in the interfacial region.

3.2. Interface fractography

It is well known that the failure mode is one of the most important characteristics of an adhesive–adherend system. On the basis of the past works [18–21], the failure mode can be divided into three kinds of failure: (a) adhesion (or interfacial) failure (see Fig. 5a; rupture of the adhesive bond, such that separation appears to occur along one of the two adhesive–adherend interfaces), (b) cohesive failure (see Fig. 5b; rupture of the adhesive bond, such that the separation appears to be within the bulk of the adhesive layer) and (c) mixed failure (see Fig. 5c; crack propagates partly between the adhesive and adherend and partly through the adhesive and/or adherend).

Fracture surfaces of ACF joints subjected to hydrothermal environments at various accelerated aging times are shown in Fig. 6, in order to further investigate the effect

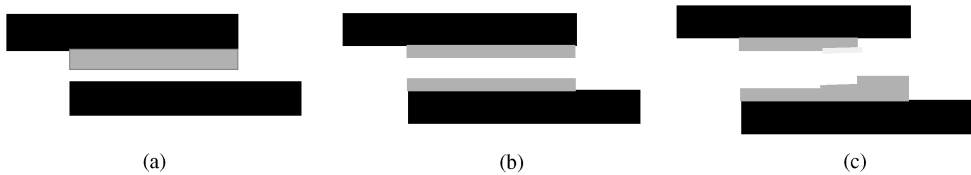


Figure 5. Types of failures in adhesively bonded joints: (a) interfacial failure; (b) cohesive failure; (c) mixed failure.

of the hygrothermal aging on the fracture mechanisms of ACF joints. Figure 6 presents SEM micrographs of fracture surfaces at hygrothermal aging times of 0, 125, 250, 375 and 550 h, respectively. In Fig. 6, the small white balls are the fine conductive particles and dark areas are the dents left by the conductive particles, while the other materials represent the thermosetting epoxy matrix.

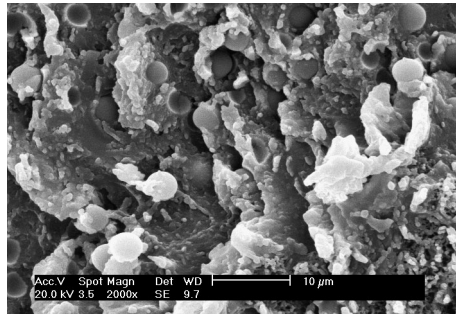
Fractographic analysis results show that the ACF joints lose their ductility and yield a relatively flat fracture surface as the accelerated time increases, which means that a transition from interfacial to cohesive mode of debonding occurred. For the unaged sample (see Fig. 6a), the scanning electron fractograph shows a moderately ductile fracture of adhesive due to shear loading, because there is no relatively flat fracture surface and parts of the adhesive are elongated, i.e., the rupture of the adhesive bond (the separation appears to be within the bulk of the adhesive layer). This is mainly attributed to the cohesive failure mode. With increasing aging time (Fig. 6b–e), the areas of relatively flat fracture surfaces increase and the ductile fracture is less and less obvious. In other words, the mixed failure mode (i.e., both interfacial and cohesive failure modes) is dominant in these conditions. Due to the effect of the hygrothermal environment, the bond strength between the ACF and chip or glass substrate decreases. Brittle fracture takes place with rapid crack propagation, and the deformation becomes less obvious. Thus, it can be concluded that the fracture surfaces of ACF joints were smoother and with low plastic deformation.

4. THEORETICAL ANALYSIS

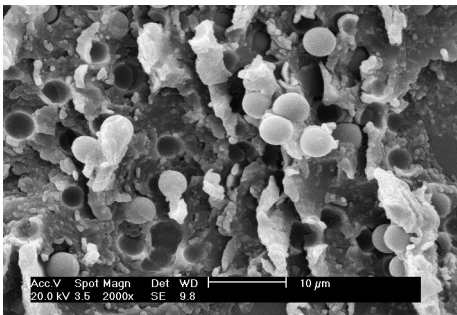
4.1. Derivation of fundamental formulas

Before starting the derivations, the following assumptions were made for simplicity [22, 23]:

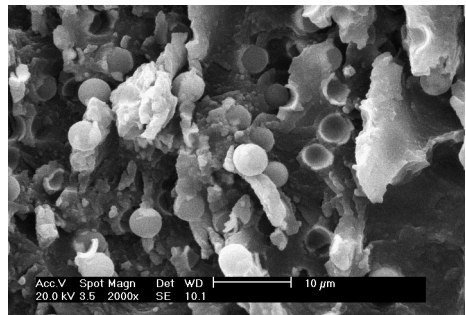
- Adherends are homogeneous and linear elastic
- Adhesive is exposed only to shear forces
- Bending effects are neglected
- Normal stresses are uniformly distributed over the cross-section
- Thickness and width of the adherends are constant throughout the bondline



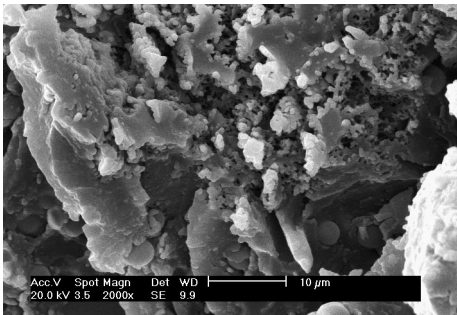
(a)



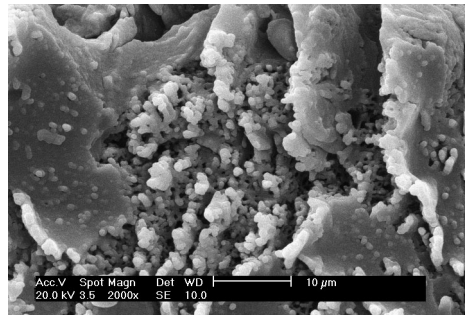
(b)



(c)



(d)



(e)

Figure 6. SEM micrographs showing changes in the shear fracture surface with hydrothermal aging (85°C/85% RH). (a) Hydrothermal aging time 0 h; (b) hydrothermal aging time 125 h; (c) hydrothermal aging time 250 h; (d) hydrothermal aging time 375 h; (e) hydrothermal aging time: 550 h.

- The interfacial fracture energy parameter is introduced to describe fracture behavior of the ACF joints with hydrothermal aging time

According to the design of the experiments, the ACF joint model for COG assemblies can be established as shown in Fig. 7. If the bending effects are ignored, the adhesive layer can be regarded as mainly subjected to shear load (mode-II fracture). The thickness and width of the layers are t_1 and b_1 for adherend 1 (Die),

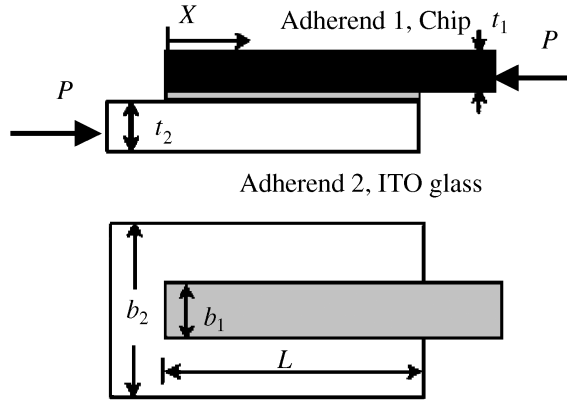


Figure 7. ACF joint model of a COG assembly.

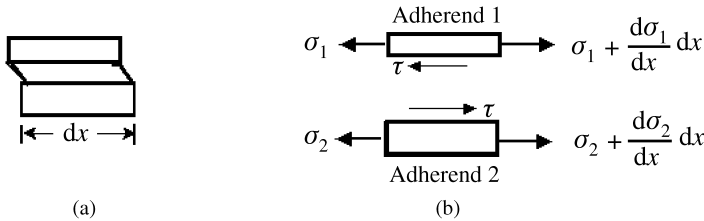


Figure 8. Deformation and stresses analysis of ACF joint: (a) deformation; (b) stresses.

and t_2 and b_2 for adherend 2 (ITO glass). The Young’s moduli of adherend 1 and adherend 2 are E_1 and E_2 , respectively, and L is the bond length.

Considering the element shown in Fig. 8, the equations of equilibrium for the adherends can be written as:

$$\frac{d\sigma_1}{dx} - \frac{\tau}{t_1} = 0, \tag{1}$$

$$\sigma_1 t_1 b_1 + \sigma_2 t_2 b_2 = P, \tag{2}$$

in which P represents the shear load and τ is local shear stress. σ_1 and σ_2 are the normal stresses for the adherends 1 and 2, respectively.

Generally, four local shear stress–slip models are used to investigate the distributions of interfacial strain or stress [24–26]. Model I, linearly increasing branch with sudden stress drop at the ultimate state; Model II, linearly increasing branch followed by linearly decreasing branch; Model III, linearly decreasing branch; and Model IV, exponentially decreasing branch. From the experimental results in this work (see Fig. 4), Model I is the best one to describe the non-linear interfacial behavior of ACF-bonded joints, as shown in Fig. 9. It is noted that the area under the τ – δ curve represents the interfacial fracture energy, G_f , which is defined as the energy required to bring a local bonding element to shear fracture, τ_f is the local bond strength, and δ_f is the maximum slip. Correspondingly, for the hygrothermally

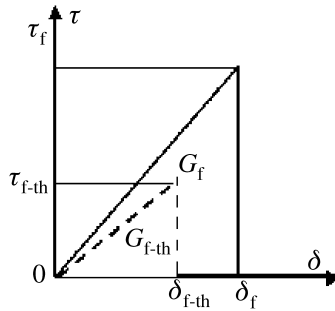


Figure 9. Simplified local shear stress–slip model for the ACF joint.

aged samples, the interfacial fracture energy, local bond strength and maximum slip are denoted as G_{f-th} , τ_{f-th} and δ_{f-th} , respectively. The simplified shear stress–slip relationship can be expressed as

$$f(\delta) = \begin{cases} \frac{\tau_f^2}{2G_f} \delta & 0 \leq \delta \leq \delta_f \\ 0 & \delta_f < \delta. \end{cases} \tag{3}$$

The slip deformation δ is defined as the relative displacement of the adherends, which is a function of the location x :

$$\delta = u_1(x) - u_2(x), \tag{4}$$

in which $u_1(x)$ and $u_2(x)$ are the displacements of adherends 1 and 2, respectively.

The constitutive equations for the adhesive layer and the two adherends are expressed as

$$\tau = f(\delta), \tag{5}$$

$$\sigma_1 = E_1 \frac{du_1(x)}{dx}, \tag{6a}$$

$$\sigma_2 = E_2 \frac{du_2(x)}{dx}. \tag{6b}$$

Equation (4) can be written in the form of the following differential equation.

$$\frac{d\delta}{dx} = \frac{du_1(x)}{dx} - \frac{du_2(x)}{dx}. \tag{7}$$

Substituting equations (2) and (6) into equation (7) gives

$$\begin{aligned} \frac{d\delta}{dx} &= \frac{du_1(x)}{dx} - \frac{du_2(x)}{dx} \\ &= \frac{\sigma_1}{E_1} - \frac{\sigma_2}{E_2} = \frac{\sigma_1}{E_1} + \frac{\sigma_1 t_1 b_1}{E_2 t_2 b_2} - \frac{P}{E_2 t_2 b_2} \end{aligned} \tag{8}$$

Therefore,

$$\sigma_1 = \left(\frac{d\delta}{dx} + \frac{P}{E_2 t_2 b_2} \right) / \left(\frac{1}{E_1} + \frac{t_1 b_1}{E_2 t_2 b_2} \right). \tag{9}$$

Substituting equations (5)–(9) into equation (1) gives

$$\frac{d^2\delta}{dx^2} - \frac{2G_f}{\tau_f^2} \lambda^2 f(\delta) = 0, \tag{10}$$

$$\sigma_1 = \frac{\tau_f^2}{2G_f t_1 \lambda^2} \left(\frac{d\delta}{dx} + \frac{P}{E_2 t_2 b_2} \right), \tag{11}$$

$$\lambda^2 = \frac{\tau_f^2}{2G_f} \left(\frac{1}{E_1 t_1} + \frac{b_1}{E_2 t_2 b_2} \right). \tag{12}$$

By substituting equation (3) into equation (10), the following equation is obtained.

$$\frac{d^2\delta}{dx^2} - \lambda^2 \delta = 0. \tag{13}$$

The relative shear displacement, shear stress of the adhesive layer, and normal stress of the substrate can be written in the following forms by solving the above differential equation (13).

$$\delta = A \sinh(\lambda x) + B \cosh(\lambda x), \tag{14}$$

$$\tau = \frac{\tau_f^2}{2G_f} (A \sinh(\lambda x) + B \cosh(\lambda x)), \tag{15}$$

$$\sigma_1 = \frac{\tau_f^2}{2G_f t_1 \lambda} \left(A \cosh(\lambda x) + B \sinh(\lambda x) + \frac{P}{\lambda E_2 t_2 b_2} \right), \tag{16}$$

with the boundary conditions

$$\begin{aligned} \sigma_1 &= 0 & x &= 0 \\ \sigma_1 &= \frac{P}{t_1 b_1} & x &= L \quad (L \text{ is the bond length}). \end{aligned} \tag{17}$$

The unknown constants in equations (14)–(16) can be obtained by substituting the boundary conditions

$$A = -\frac{P}{\lambda E_2 t_2 b_2} \quad B = \frac{P}{\lambda E_2 t_2 b_2 \tanh(\lambda L)} + \frac{P}{\lambda E_1 t_1 b_1 \sinh(\lambda L)}.$$

Then, the following results can be obtained by substituting the values of *A* and *B* into equations (14)–(16).

$$\delta = \frac{P}{\lambda} \left(\frac{1}{E_2 t_2 b_2 \tanh(\lambda L)} + \frac{1}{E_1 t_1 b_1 \sinh(\lambda L)} \right) \times \cosh(\lambda x) - \frac{P}{\lambda E_2 t_2 b_2} \sinh(\lambda x), \tag{18}$$

$$\tau = \frac{\tau_f^2}{2G_f} \left\{ \frac{P}{\lambda} \left(\frac{1}{E_2 t_2 b_2 \tanh(\lambda L)} + \frac{1}{E_1 t_1 b_1 \sinh(\lambda L)} \right) \cosh(\lambda x) - \frac{P}{\lambda E_2 t_2 b_2} \sinh(\lambda x) \right\}, \tag{19}$$

$$\sigma_1 = P \left\{ \left(\frac{1}{E_1 t_1 b_1 \sinh(\lambda L)} + \frac{1}{E_2 t_2 b_2 \tanh(\lambda L)} \right) \times \sinh(\lambda x) - \frac{1}{E_2 t_2 b_2} \cosh(\lambda x) + \frac{1}{E_2 t_2 b_2} \right\} \frac{\tau_f^2}{2G_f t_1 \lambda^2}. \tag{20}$$

From equation (18), the relation between the loadings and the values of slip at both ends are given as:

$$\begin{cases} P = \frac{\lambda E_1 t_1 b_1 E_2 t_2 b_2 \sinh(\lambda L)}{E_1 t_1 b_1 \cosh(\lambda L) + E_2 t_2 b_2} \times \delta & x = 0 \\ P = \frac{\lambda E_1 t_1 b_1 E_2 t_2 b_2 \sinh(\lambda L)}{E_1 t_1 b_1 + E_2 t_2 b_2 \cosh(\lambda L)} \times \delta & x = L. \end{cases} \tag{21}$$

4.2. Effect of hygrothermal environment on interfacial fracture energy

From equation (21), it can be found that there is a linear relation between the loadings and the values of slip at both ends. If the linear data fit methods are applied to the experimental results (shown in Fig. 4), the following expressions are obtained:

Hygrothermal aging time (h)	Fit equation
0	$P = 2725.0967 \times \delta - 7.7015$
125	$P = 2568.6046 \times \delta - 7.6075$
250	$P = 2396.2468 \times \delta - 7.4510$
375	$P = 2302.7667 \times \delta - 7.2650$
550	$P = 2163.0134 \times \delta - 6.7601$

Comparing equation (21) and equation (22), it can be easily found that the difference between them is that equation (22) has constant terms. Due to the system errors or error in precision of the test machine (such as clearance of the test machine), the first small fractions of shear force–cross-head displacement curves (Fig. 4) are slightly nonlinear and, thus, the constant terms appear. Substituting the

Table 2.

Main parameters of materials used

Parameter	Adherend 1 (chip)	Adherend 2 (ITO glass)	ACF
Young's modulus, E (MPa)	128000	68600	1450
Poisson's ratio, ν	0.3	0.28	0.24
Layer thickness, t (mm)	0.4	0.5	0.025
Layer width, b (mm)	1.6	15	1.6

material parameters (shown in Table 2) and the bond length ($L = 6.5$ mm) into equation (12), the interfacial fracture energy at different hygrothermal aging times can be obtained as follows.

$$\begin{array}{l}
 \text{Hygrothermal aging time (h)} \\
 0 \\
 125 \\
 250 \\
 375 \\
 550
 \end{array}
 \left.
 \begin{array}{l}
 \text{Interfacial fracture energy} \\
 G_{f-0} = 3.9146 \text{ N} \cdot \text{mm}/\text{mm}^2 \\
 G_{f-125} = 3.6301 \text{ N} \cdot \text{mm}/\text{mm}^2 \\
 G_{f-250} = 2.9421 \text{ N} \cdot \text{mm}/\text{mm}^2 \\
 G_{f-375} = 2.3178 \text{ N} \cdot \text{mm}/\text{mm}^2 \\
 G_{f-550} = 2.0672 \text{ N} \cdot \text{mm}/\text{mm}^2
 \end{array}
 \right\} . \quad (23)$$

It is obvious that the interfacial fracture energy decreases with the increase of hygrothermal aging time. In order to further investigate the decrease of interfacial fracture energies, a dimensionless parameter (A) is introduced, i.e.,

$$A = \frac{G_f - G_{f-\text{th}}}{G_f}, \quad (24)$$

where $G_{f-\text{th}}$ is the interfacial fracture energy for the samples subjected to hygrothermal aging, while G_f is the interfacial fracture energy for those samples prior to the accelerated aging. Based on the above values of interfacial fracture energies obtained from the experiments, the dimensionless parameter (A) can be calculated for different hygrothermal aging times, i.e., 125, 250, 375, and 550 h, as shown in Fig. 10.

From Fig. 10, it can be easily seen that the dimensionless parameter (A) gradually increases at first, then quickly increases and finally the rate of increase slows down again with increasing hygrothermal aging. Thus, it can be concluded that the interfacial fracture energy has the reverse evolution regularity based on equation (24). The process of degradation for the interfacial fracture energy can be approximately divided into three phases, i.e., the primary, secondary and tertiary phases. In the primary phase, the rate of decrease of the interfacial fracture energy is relatively low. From the conclusions in Section 3.2, it can be deduced that the bond strengths of COG assemblies mainly result from the degradation of the ACF materials, and the main failure mode of ACF joints is a cohesive failure in the

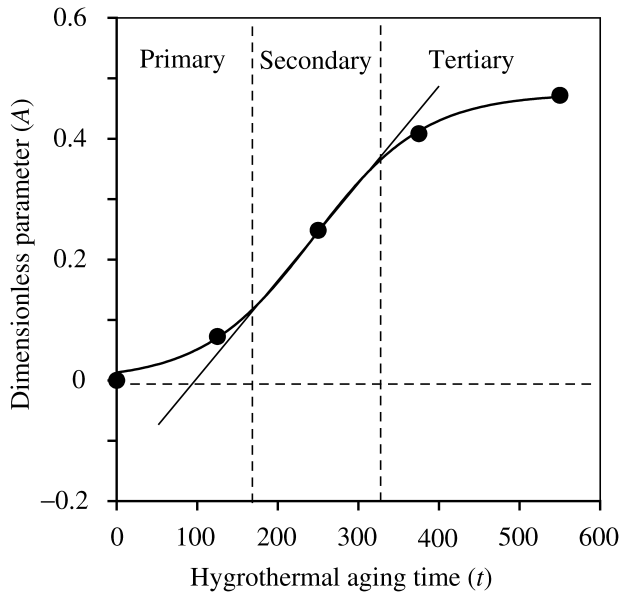


Figure 10. Relation between the dimensionless parameter A and hydrothermal aging time: the symbols represent the values of dimensionless parameter A at various hydrothermal aging times; the bold solid line represents the results of data fitting; the thin line shows the linear relation between the dimensionless parameter A and hydrothermal aging time in the secondary phase.

primary phase. In the secondary phase, the interfacial fracture energy decreases fast, due to the combined effect of the degradation of the ACF materials and the damage to the interfaces under the hydrothermal conditions. Also, the experiments show the interfacial failure mode is more and more obvious. In the tertiary phase, the interfacial fracture energy tends to a state of saturation, and the rate of decrease of the interfacial fracture energy is lower than in the previous two phases.

If data fittings are performed on the above-calculated results (the dimensionless parameter A for the different hydrothermal aging times) by the following equation, the relation between the dimensionless parameter A and hydrothermal aging time can be obtained as,

$$A = \frac{a}{1 + e^{-k(t-b)}}, \quad (25)$$

in which a , b and k constants: $a = 0.475$, $b = 244.838$, $k = 0.015$.

From equation (24) and $G_{f-0} = 3.9146 \text{ N mm/mm}^2$, the change in the interfacial fracture energy with hydrothermal aging time (t), is expressed as:

$$G_{f-\text{th}} = 3.9146 - \frac{1.859}{1 + e^{-0.015(t-244.838)}}. \quad (26)$$

4.3. Verification of fundamental formulas

In order to verify the above fundamental theoretical derivation and analysis, the relation between the interfacial fracture energy and the hygrothermal aging time obtained from the samples with a bond length of 6.5 mm, is applied to the other samples with bond length of 8 mm. The theoretical relation between the shear force and the slip displacement at the end of the chip can be obtained by equation (21), as shown in Fig. 11. The experimental results for the samples with a bond length of 8 mm are also given in Fig. 11, to compare with the calculated results. It is evident that there is a good agreement between the experimental and calculated results, except for a slight difference in the initial phase of hygrothermal aging. This difference may result from the system errors or error in precision of the test machine, such as clearance of the test machine.

4.4. Distribution of interfacial stress

According to equations (19) and (20), the distributions of shear stress in the bonding layer can be obtained for the different hygrothermal aging times, i.e., 0, 125, 250, 375 and 550 h. Figure 12 shows the shear stress distributions for the samples with a bond length of 6.5 mm. It can be found that the shear stress in the bonding layer gradually decreases with the increase of accelerated aging time, which means the reliability of the ACF joints of COG assemblies gradually decreases.

5. CONCLUSIONS

In this study, the effects of aging on epoxy-based anisotropic conductive adhesive film (ACF) joints in chip-on-glass (COG) assemblies were investigated by shear tests, scanning electron microscopy (SEM) and theoretical analysis. The results show that: (1) the ACF adhesion strength decreases with aging, i.e., the reliability of the ACF joints of COG assemblies gradually decreases; (2) the fracture mechanism of ACF joints gradually changes with hygrothermal aging. ACF joints lose their ductility and yield a relatively flat fracture surface as the accelerated time increases, showing a transition from interfacial to cohesive mode of debonding; and (3) it is reasonable to establish a mechanics model by introducing a dimensionless parameter A , which is obtained from the interfacial fracture energy, and the process of degradation of the interfacial fracture energy can be approximately divided into three phases, namely primary, secondary and tertiary phases.

Acknowledgements

The authors gratefully acknowledge financial support for this work from the National Natural Science Foundation of China (No.50528506) and the Teaching and Research Award Program for Outstanding Young Teachers in Higher Education Institutions of MOE, P.R. China.

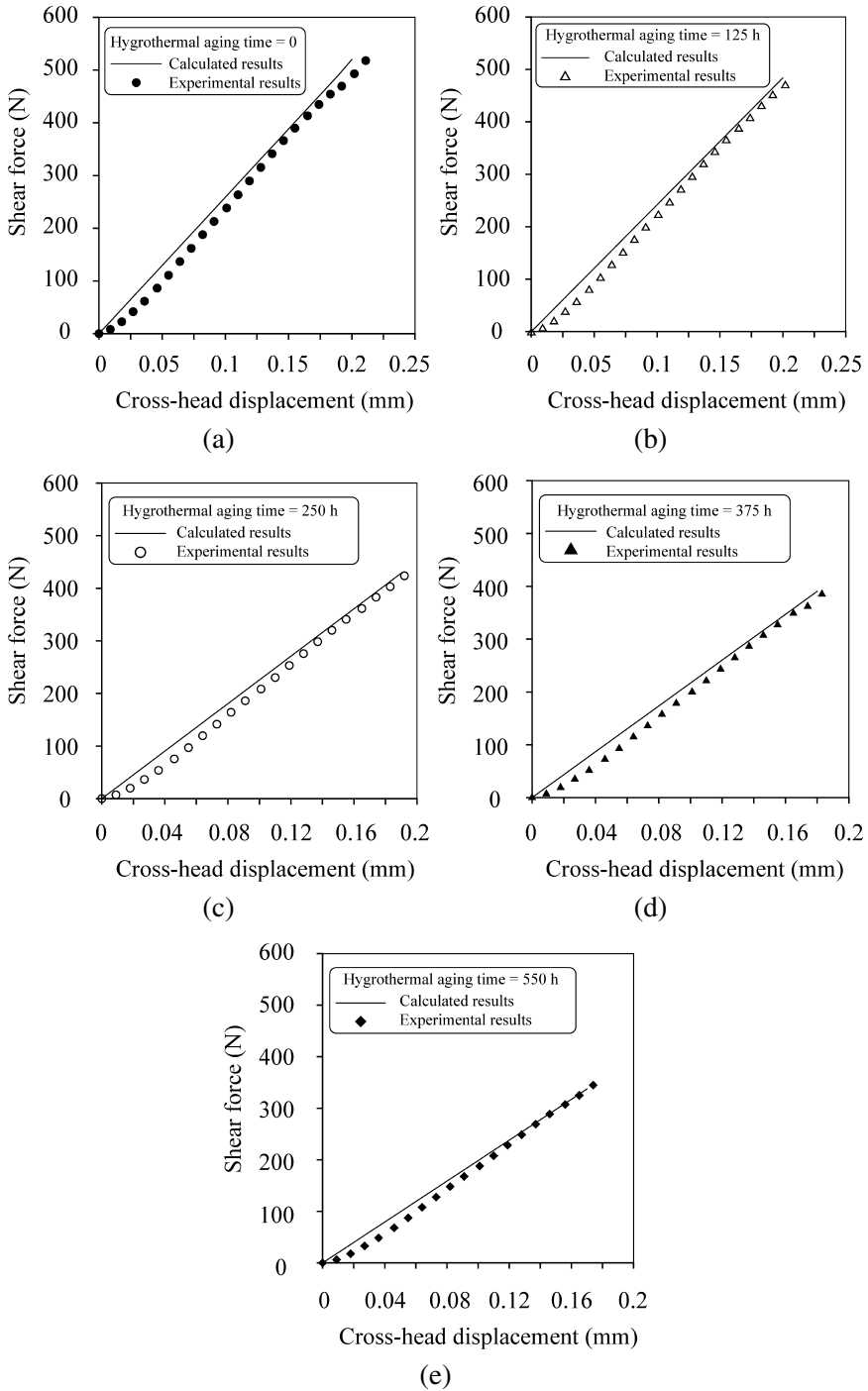


Figure 11. Comparison of experimental and calculated results (bond length $L = 8$ mm) for a hydrothermal aging time of (a) 0 h; (b) 125 h; (c) 250 h; (d) 375 h; (e) 550 h.

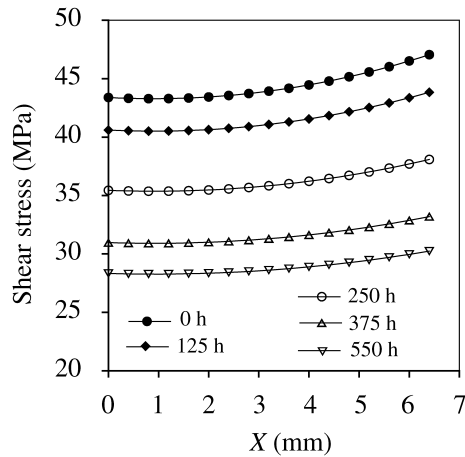


Figure 12. Distribution of shear stress in the bond layer with hygrothermal aging (X represents the distance from the left end of the bond length, as shown in Fig. 7).

REFERENCES

1. Y. Li, K. Moon and C. P. Wong, *J. Electronic Mater.* **34**, 267–271 (2005).
2. J. Liu, *Solder Surface Mount Technol.* **13**, 39–57 (2001).
3. C. W. Tan, Y. C. Chan and N. H. Yeung, *Microelectron. Reliab.* **43**, 279–285 (2003).
4. E. H. Wong, R. Rajoo, S. W. Koh and T. B. Lim, *J. Electron. Packag.* **124**, 122–126 (2002).
5. S. O. Han and L. T. Drzal, *Eur. Polym. J.* **39**, 1791–1799 (2003).
6. Y. C. Lin and X. Chen, *Polymer* **46**, 11994–12003 (2005).
7. Y. C. Lin and X. Chen, *Mater. Lett.* **59**, 3831–3836 (2005).
8. Y. C. Lin and X. Chen, *Chem. Phys. Lett.* **412**, 322–326 (2005).
9. Y. Li and H. J. Sue, *Polym. Eng. Sci.* **42**, 375–381 (2002).
10. S. Luo and C. P. Wong, *J. Adhesion Sci. Technol.* **18**, 275 (2004).
11. S. Luo and C. P. Wong, *IEEE Trans. Component. Packag. Technol.* **24**, 38–42 (2001).
12. T. Sawa, J. Liu, Y. Nakano and J. Tanaka, *J. Adhesion Sci. Technol.* **14**, 43–66 (2000).
13. I. Higuchi, T. Sawa and H. Suga, *J. Adhesion Sci. Technol.* **16**, 1327–1342 (2002).
14. L. Higuchi, T. Sawa and H. Suga, *J. Adhesion Sci. Technol.* **16**, 1585–1602 (2002).
15. T. Sawa, L. Higuchi and H. Suga, *J. Adhesion Sci. Technol.* **17**, 2157–2174 (2003).
16. S. K. Karad, F. R. Jones and D. Attwood, *Polymer* **43**, 5209–5218 (2002).
17. M. R. Vanlandingham, R. F. Eduljee and J. W. Gillespie Jr., *J. Appl. Polym. Sci.* **71**, 787–798 (1999).
18. M. Davis and D. Bond, *Int. J. Adhesion Adhesives* **19**, 91–105 (1999).
19. R. Balkova, S. Holcnerova and V. Cech, *Int. J. Adhesion Adhesives* **22**, 291–295 (2002).
20. M. A. Ansarifar, J. Zhang, J. Baker, A. Bell and R. J. Ellis, *Int. J. Adhesion Adhesives* **21**, 369–380 (2001).
21. Y. J. Weitsman, *J. Composite Mater.* **11**, 378–394 (1977).
22. B. Täljsten, *Int. J. Fract.* **82**, 253–266 (1996).
23. B. Täljsten, *J. Mater. Civil Eng.* **9**, 206–212 (1997).
24. J. Jia, T. E. Boothby, C. E. Bakis and T. L. Brown, *J. Compos. Constr.* **9**, 348–359 (2005).
25. H. Yuan, Z. S. Wu and H. Yoshizawa, *J. Struct. Mech. Earthquake Eng.* **18**, 27–39 (2001).
26. J. F. Chen and J. G. Teng, *J. Struct. Eng.* **127**, 784–791 (2001).